Available online at www.sciencedirect.com
ScienceDirect
Journal of Sound and Vibration 301 (2007) 297–318
JOURNAL OF SOUND AND VIBRATION
www.elsevier.com/locate/jsvi

# Active control of resiliently mounted beams using triangular actuators

Chinsuk Hong*, Paolo Gardonio, Stephen J. Elliott

*Institute of Sound and Vibration, University of Southampton, Highfield, Southampton, SO17 1BJ, UK*

Received 4 April 2006; received in revised form 14 July 2006; accepted 10 October 2006
Available online 11 December 2006

**Abstract**

This paper is concerned with the use of triangularly shaped actuators for the implementation of direct velocity feedback (DVFB) control on a resiliently mounted beam. The effects on the stability is investigated of boundary conditions and the shape of the actuator. For practical boundary conditions, with a combination of the rotational and linear springs, it is found that the linear spring is the principal component affecting the stability and thus the control performance. The stiffness of this spring has to be high enough to approximate a simply supported boundary condition for good performance.

The amplitude of the sensor–actuator frequency response function increases as the top angle and the height of the triangular actuator is increased so that control effort can be saved. However, as the height of the actuator is increased, the stability margin reduces. Therefore, for the given beam there is an actuator shape that gives the best compromise between the stability and control effort.


## 1. Introduction

Control of low-frequency sound transmission through lightly damped and lightweight panels in aircrafts, helicopters, automobiles and trains is an important design issue. The sound transmission at low frequencies can be reduced by controlling the response of the panel itself and by modifying the radiation efficiency of the low-frequency resonant modes [1]. For example, mass and stiffness treatments can be used both to reduce vibration and to modify the sound radiation efficiency of low-order modes in order to produce an overall reduction of the sound radiation. However, these passive techniques have limited performance at low frequencies and require substantial variation to the structure of the panel causing drawbacks such as the change of geometry and weight and the increase of costs [2]. Alternatively, active control techniques could be employed using sensor/actuator transducers connected by an active controller which may be decentralised. Vibration actuators can be divided into two main categories: force actuators and strain actuators. A point velocity sensor and a force actuator can easily form a collocated and dual sensor–actuator pair which is particularly convenient for the local implementation of stable direct velocity feedback control loops. However,

*Corresponding author. Tel.: +44 2380 594932; fax: +44 2380 593190.
*E-mail addresses:* csh@isvr.soton.ac.uk (C. Hong), pg@isvr.soton.ac.uk (P. Gardonio), sje@isvr.soton.ac.uk (S.J. Elliott).

0022-460X/$ - see front matter © 2006 Elsevier Ltd. All rights reserved.
doi:10.1016/j.jsv.2006.10.013

in order to generate a point force, the actuator must react against another structure or against a proof mass. Thus, this configuration tends to be heavy and occupy large volumes. To achieve compact and lightweight smart panels, strain actuators have been considered. Normally square piezoelectric patch actuators with accelerometer sensor at their centre have been used to implement direct velocity feedback control [3–6]. With this configuration, however, it is a problem to ensure unconditionally stable feedback loops because the sensor–actuator pair is not truly collocated and dual. Furthermore, the actuation obtained from the piezo-patch is a distribution of moments along the edges, which more effectively couples into higher modes of the structure than lower ones, so that the sensor–actuator frequency response function has large amplitude at higher frequencies where the phase exceed $-90^\circ$ and thus the closed loop is likely to become instable for large control gains.

Recently, Gardonio and Elliott [2] have proposed the use of triangularly shaped piezo-actuators arranged along the perimeter of the radiating structure with accelerometers at their top vertexes. In this context they found that the configuration gives much larger gain margin and better performance than using the square patches on a simply supported plate. Since in practice the boundary condition is not perfectly simply supported, more understanding about the force and moments generated by the triangularly shaped piezoceramic actuator on a structure with compliant boundaries is required. Indeed the aim of this paper is to investigate the effects of compliant boundary conditions on the stability and control performance of a velocity feedback loop using a triangularly shaped actuator aligned along the border of a thin structure. In order to provide a clear understanding of the principal phenomena which determine the stability and performance of such a system, a simple model problem is considered, which is made of a thin beam with transverse and rotational springs at the ends and has one triangularly shaped piezoelectric actuator with the base located at one end of the beam. Many researchers [7–9] have used a triangularly shaped actuator to approximate a linear shading of a piezoelectric actuator in one dimension which gives transverse point force at both ends and a moment at the one end. In the previous applications [7–9], however, a very long triangular actuator covering whole length of a cantilever beam has been used such that the actuator angle was very small, e.g. $\theta_{PZT} < 4.3^\circ$ in Ref. [9]. In this case the contribution of the moment distribution along the lateral sides is negligible.

In Section 2, the response of a resiliently mounted beam supported by both linear and rotational springs at both ends is examined. Based on the formulation of a generally distributed piezoceramic patch [10,11], the actuation resultant due to a triangularly shaped piezoceramic actuator on the beam is derived in Section 3. The implementation of a direct velocity feedback control system using the triangularly shaped actuator is then studied in Section 4. The effects of the boundary conditions are evaluated and the boundary condition requirements for a stable feedback control loop are analysed. Finally, a parametric study on the shapes of the actuators is made in Section 6 with reference to the stability and controllability.

## 2. Resiliently mounted beams with a triangularly shaped actuator

In this section the response of a resiliently supported beam is modelled and analysed. As shown in Fig. 1, a general resilient boundary condition can be modelled by a rotational spring and a linear spring at each end. Assuming Euler–Bernoulli beam theory, which is valid for slender beams e.g. flexible wavelengths are greater than 10 times the larger cross-section dimension, the equation of motion for the forced lateral vibration [12,13] is given by

$$E(1+\mathrm{j}\eta)I\,\frac{\partial^4 w}{\partial x^4}(x,t)+\rho A\,\frac{\partial^2 w}{\partial t^2}(x,t)=L(x,t), \tag{1}$$

where $E$ is Young's modulus, $I$ is the moment of inertia of the beam cross-section about the $y$-axis, $\eta$ is loss factor, $\rho$ is mass density, $A$ is cross-sectional area of the beam and $L(x,t)$ is the excitation operator. It is assumed that the piezoceramic actuator is much thinner than the beam an so has negligible effect on its dynamic behaviour. When the beam is excited by a force, $f(x,t)$ and moment, $T(x,t)$, then,

$$L(x,t)=f(x,t)+\frac{\partial T}{\partial x}(x,t). \tag{2}$$

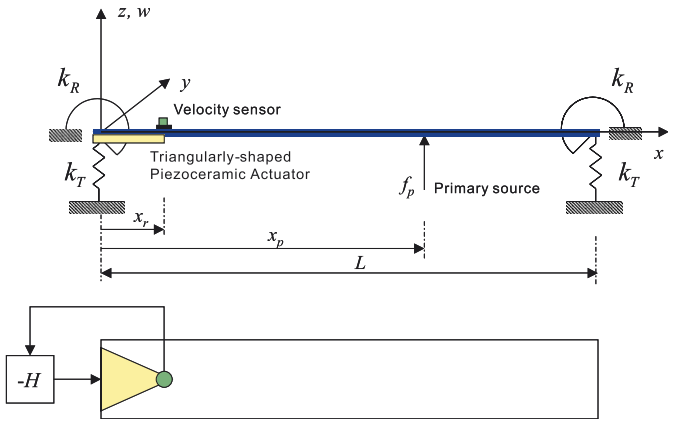


Fig. 1. Bernoulli–Euler beam with a general boundary condition, subject to forces and moments generated by a triangular actuator.

Table 1
Mechanical properties of the beam

| Symbol | Value | Descriptions |
|---|---|---|
| $E$ | 65 | Young's modulus (MPa) |
| $\rho$ | 2650 | Density (kg/m$^3$) |
| $v$ | 0.3 | Poisson ratio |
| $L$ | 0.50 | Length (m) |
| $b$ | 0.03 | Width (m) |
| $h$ | 0.002 | Thickness (m) |
| $\eta$ | 0.01 | Loss factor |

The boundary conditions resulting from the linear and rotational springs can be given by applying the moment and shear force balance at the ends of the beam. Hence, the boundary conditions are

$$\frac{\partial^2 w}{\partial x^2} = \frac{k_R}{EI}\frac{\partial w}{\partial x}, \quad \frac{\partial^3 w}{\partial x^3} = -\frac{k_T}{EI}w \tag{3}$$

at $x = 0$ and

$$\frac{\partial^2 w}{\partial x^2} = -\frac{k_R}{EI}\frac{\partial w}{\partial x}, \quad \frac{\partial^3 w}{\partial x^3} = \frac{k_T}{EI}w \tag{4}$$

at $x = L$, where $k_R$ and $k_T$ are the rotational and linear spring constants, respectively.

In order to simplify the analysis, it is convenient to define non-dimensional linear and angular spring constants as

$$\kappa = \frac{k_T L^3}{EI}, \quad \tau = \frac{k_R L}{EI}. \tag{5}$$

The free vibration response of the resiliently supported beam considered in this study has been derived using the formulation presented by Magrab [13]. The natural frequencies for the beam with dimensions and material properties given in Table 1 are examined to characterise the effects produced by the resilient boundary conditions. Fig. 2 shows the variation of the natural frequencies with the linear spring constant when $\tau = 0$ and with the rotational spring constant when $\kappa = \infty$. Fig. 2(a) shows that for very small linear and angular stiffnesses, the first two natural frequencies are approximately zero since the natural response of the beam is characterised by translational and rocking rigid body modes on the soft springs. Also, the higher order natural

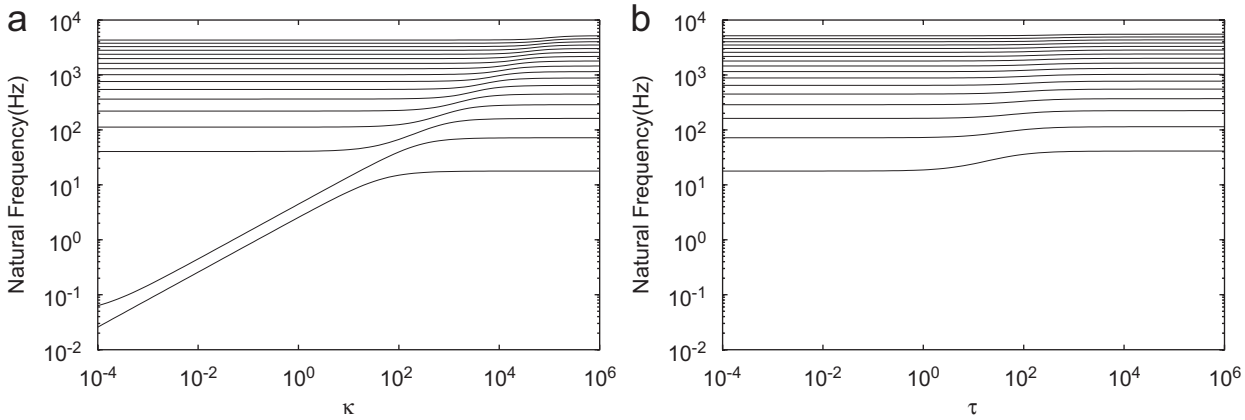


Fig. 2. Variation of natural frequencies with the spring constants: (a) when $\tau = 0$, (b) when $\kappa = \infty$.

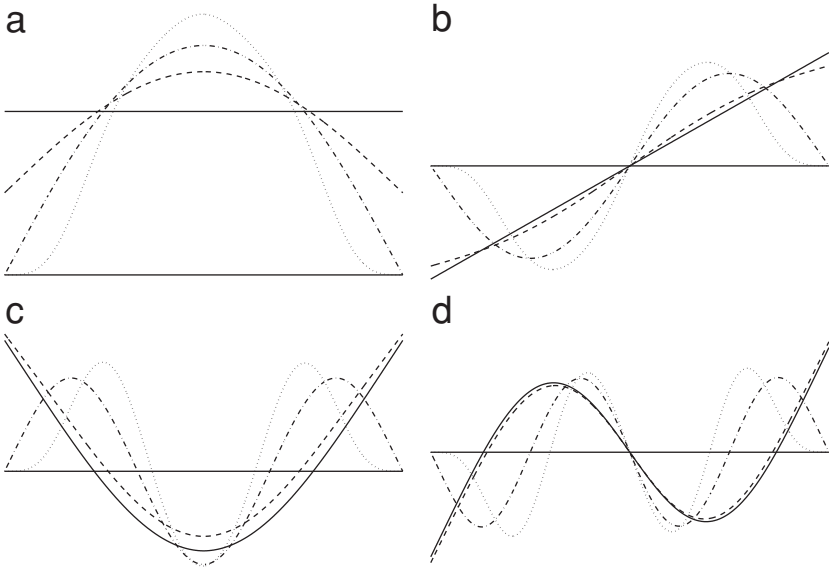


Fig. 3. Variation of natural modes with the spring constants: (a) first modes, (b) second modes, (c) third modes, and (d) fourth modes for a freely supported beam ($\kappa = 0$ and $\tau = 0$) (solid), a resiliently supported beam ($\kappa = 50$ and $\tau = 0$) (dashed), a simply supported beam ($\kappa = \infty$ and $\tau = 0$) (dot–dashed) and a clamped beam ($\kappa = \infty$ and $\tau = \infty$) (dotted).

frequencies approximate those of a flexible freely supported beam. When the linear spring constant is raised to higher values such that $\kappa \approx 10^3$, for example, then the natural frequencies change to those of a simply supported beam. Fig. 2(b) shows that, when the angular spring constant is also raised, the natural frequencies change to those of a clamped beam when $\tau \approx 10^3$. The same behaviour can be seen from the variation of the first four natural modes with the spring constants shown in Fig. 3.

## 3. Equivalent actuation on beam generated by a triangular piezo-patch

The excitation field generated by a piezoelectric patch actuator results from the elastic coupling of the actuator and the structure on which it is bonded. Assuming first-order shear deformation [10,14] in the structure, Lee [10] has formulated the flexural actuation effect on two-dimensional plate structures in terms of

the following spatial differential operator ($\mathscr{L}$):

$$\mathscr{L}[\Lambda(x,y)] = e_{31}^0 \frac{\partial^2 \Lambda(x,y)}{\partial^2 x} + e_{32}^0 \frac{\partial^2 \Lambda(x,y)}{\partial^2 y} + 2e_{36}^0 \frac{\partial^2 \Lambda(x,y)}{\partial x \partial y}, \tag{6}$$

where $\Lambda(x,y)$ is the distribution function describing the shape of the piezoelectric actuator and $e_{31}^0$, $e_{32}^0$ and $e_{36}^0$ represent the piezoelectric stress/charge constants with respect to the structure axes.

Sullivan [15] has shown that, a triangularly shaped actuator having thickness, $h_{PZT}$, and the top angle, $\theta_{PZT}$, bonded on a thin plate with thickness of $h_p$ generates forces at the three vertexes and moments along the three edges as shown in Fig. 4, which are given by

$$\begin{aligned} L(x,t) = {} & \frac{h_s v_{cs}(t)}{2}[2me_{31}^0\{\delta(x)\delta(y-b) + \delta(x)\delta(y+b) - 2\delta(x-a)\delta(y)\}] \\ & + \frac{h_s v_{cs}(t)}{2}\left[e_{31}^0\{U(y+b) - U(y-b)\}\frac{\partial\delta(x)}{\partial x}\right] \\ & - \frac{h_s v_{cs}(t)}{2}\left[(m^2 e_{31}^0 + e_{32}^0)\left\{\frac{\delta(y-mx+b)}{\partial \mathbf{n}_1} + \frac{\delta(y+mx-b)}{\partial \mathbf{n}_2}\right\}\right], \end{aligned} \tag{7}$$

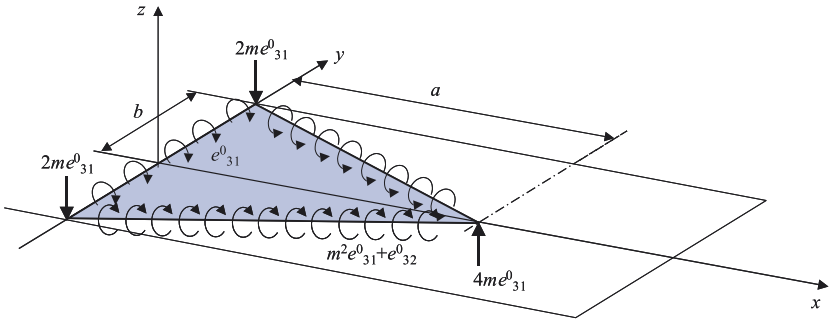


Fig. 4. Excitation field for beams due to the triangularly shaped actuator obtained from two-dimensional approach. Note that the expressions in the figure are the resultant of the Laplacian operator so that the moments and forces generated are calculated multiplying $h_s v_{cs}(t)/2$.

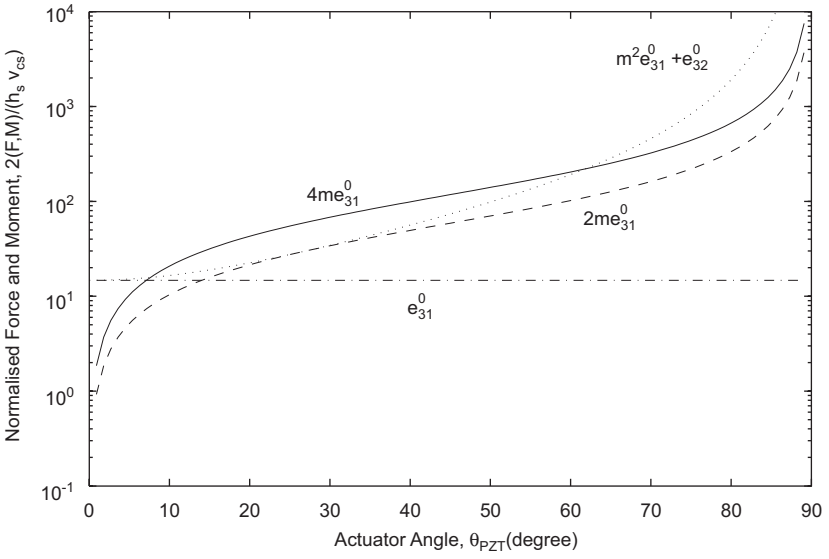


Fig. 5. Variation of actuation with the actuator angle. It is noted that the actuation components associated with $m = \tan\theta_{PZT}$ diverse.

where $h_s = (h_p + h_{PZT})/2$, $m = b/a = \tan\theta_{PZT}$, $a$ and $b$ are the height and the half-base length of the actuator, $v_{cs}$ is the voltage to the actuator, $\delta()$ and $U()$ are the delta function and the step function, respectively, and $\mathbf{n}_1$ and $\mathbf{n}_2$ are the unit normal vector of the inclined sides of the triangular actuator. Fig. 5 shows the dependence of these excitation components on the actuator top angle, $\theta_{PZT}$, for the material and piezoelectric properties summarised in Table 2. Apart from the moment excitation on the side along the $y$-axis, the force and moment excitations strongly depend on the shape of the actuator. However, the response of the structure depends on the modal coupling of the excitation field with the natural modes of the structure itself. As shown in Ref. [16], the effectiveness of the point force excitation is directly related to the modal displacement at the force location while that of the moment is related to the slope of the mode at the moment location.

The actuation components for beams can be evaluated by projecting the two-dimensional distribution, shown in Fig. 4, on the beam axes, $x$. The forces at the vertexes of the base edge of the actuator are summed up and act at the end of the beam. The line of moments along the base edge is also modelled as a concentrated moment at the end of the beam. The moments along the lateral sides generate bending and torsional excitation. The bending components along each lateral side are summed, while the torsional moments along the lateral sides cancels each other when projected on the beam axes. Therefore, the actuation components for beams with a triangularly shaped actuator at one end can be expressed as

$$\begin{aligned} L(x,t) = {} & \frac{h_s v_{cs}(t)}{2}[4me_{31}^0\{\delta(x-a)-\delta(x)\}] \\ & + \frac{h_s v_{cs}(t)}{2}\left[2be_{31}^0\,\frac{\partial\delta(x)}{\partial x}\right] \\ & - \frac{h_s v_{cs}(t)}{2}[2m(m^2e_{31}^0 + e_{32}^0)\{\delta(x)-\delta(x-a)\}]. \end{aligned} \tag{8}$$

The first term in Eq. (8) denotes the concentrated forces at $x = 0$ and $a$, the second term the concentrated moment at $x = 0$, and the third term corresponds to two concentrated forces at $x = 0$ and $a$, which originally come from the distributed moments between $x = 0$ and $a$. Physically, the distributed moments can be interpreted with pairs of forces generating the moments. Thus, apart from the forces at the boundary, the internal force components of neighbour pairs cancel each other. Hence, assuming that $d_{3'1'} = d_{3'2'}$ and $d_{3'6'} = 0$, the equivalent actuation resultant on a beam generated by the triangular piezoelectric patch bonded at one end of the beam is given by one concentrated moment at $x = 0$ and two concentrated forces at $x = 0$ and $a$, as shown in Fig. 6, so that

$$L(x,t) = me_{31}^0 h_s v_{cs}(t)\left[(m^2+3)\{\delta(x-a)-\delta(x)\} + a\,\frac{\partial\delta(x)}{\partial x}\right] \tag{9}$$

for which the relationship, $b = a\tan\theta_{PZT} = ma$, is used.

In general the response of beams to force and moment excitations can be calculated by substituting the excitation components, $L(x,t)$, into the wave Eq. (1) together with the boundary conditions. Using the modal

Table 2
Geometry and physical parameters assumed for the piezoelectric actuator

| Parameters | Symbol | Values |
|---|---|---|
| Thickness (mm) | $h_{PZT}$ | 1.0 |
| Young's modulus (GPa) | $Y_{PZT}$ | 63 |
| Density (kg/m$^3$) | $\rho_{PZT}$ | 7600 |
| Poisson ratio | $\nu_{PZT}$ | 0.29 |
| Piezoelectric stress/charge constants (V/m (or C/N)) | $d_{3'1'}^0$ | $166\times10^{-12}$ |
| | $d_{3'2'}^0$ | $166\times10^{-12}$ |
| | $d_{3'6'}^0$ | 0 |

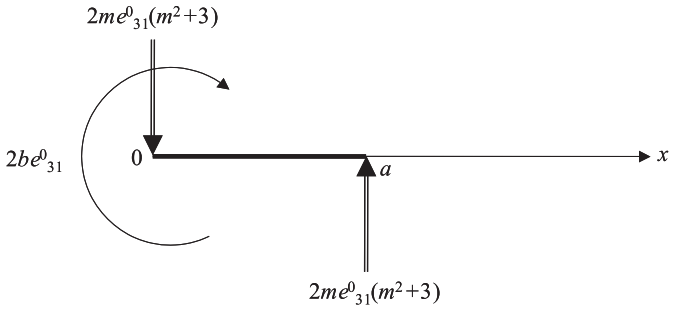


Fig. 6. Equivalent actuation resultant for beams with a triangular actuator. Note that the expressions in the figure are the resultant of the Laplacian operator so that the moments and forces generated are calculated multiplying $h_s v_{cs}(t)/2$.

summation expansion [17] as

$$\dot{w}(x,t) = \sum_n \phi_n(x) a_n(t), \tag{10}$$

then, because of the orthogonality of modes,

$$a_n(t) = A_n(F_n + T_n), \tag{11}$$

where

$$F_n(t) = \int_0^L \phi_n(x) f(x,t)\,\mathrm{d}x, \quad T_n(t) = \int_0^L \frac{\partial T(x,t)}{\partial x}\phi_n(x)\,\mathrm{d}x \tag{12}$$

and

$$A_n(\omega) = \frac{\mathrm{j}\omega}{\rho A L[(1+\mathrm{j}\eta)\omega_n^2 - \omega^2]}. \tag{13}$$

Thus, we can now obtain the responses to the primary force, $f_p(x,t) = F_p\delta(x-x_p)\exp(\mathrm{j}\omega t)$ and the piezo secondary excitations generated by the driving voltage, $v_{cs}(t) = V_{cs}\exp(\mathrm{j}\omega t)$ as

$$\dot{w}_p(x,\omega) = Y_{xp}(x,\omega)F_p \quad \text{and} \quad \dot{w}_s(x,\omega) = Y_{xs}(x,\omega)V_{cs}, \tag{14}$$

where

$$Y_{xp}(x,\omega) = \mathbf{\Phi}(x)\mathbf{a}_p(\omega) \quad \text{and} \quad Y_{xs}(x,\omega) = \mathbf{\Phi}(x)\mathbf{a}_s(\omega). \tag{15}$$

$\mathbf{\Phi}(x)$ is row vectors with the first $R$ flexural natural modes of the beam given by

$$\mathbf{\Phi}(x) = [\phi_1(x)\ \ \phi_2(x)\ \ \ldots\ \ \phi_R(x)] \tag{16}$$

and $\mathbf{a}_p(\omega)$ and $\mathbf{a}_s(\omega)$ are column vectors of the excitation terms of the first $R$ flexural natural modes of the beam due to the primary force and the secondary excitations generated by the triangular piezo patch, respectively:

$$\mathbf{a}_p(\omega) = \begin{bmatrix} a_{p,1} \\ a_{p,2} \\ \vdots \\ a_{p,R} \end{bmatrix} \quad \text{and} \quad \mathbf{a}_s(\omega) = \begin{bmatrix} a_{s,1} \\ a_{s,2} \\ \vdots \\ a_{s,R} \end{bmatrix}. \tag{17}$$

The terms in the excitations vectors are given by

$$a_{p,n}(\omega) = A_n(\omega)\phi_n(x_p), \tag{18}$$

$$a_{s,n}(\omega) = A_n(\omega)me_{31}^0 h_s[(m^2+3)\{\phi_n(a) - \phi_n(0)\} - a\phi_n'(0)]. \tag{19}$$

## 4. Direct velocity feedback control for beams using a triangular actuator: stability

Fig. 7 shows the block diagram of the feedback loop implemented at the end of a beam with a triangular piezoelectric patch actuator and velocity sensor pair shown in Fig. 1. The feedback gain will be assumed to be constant so that direct velocity feedback control is implemented. The total velocity response at the sensor location, $x = a$, can be expressed as

$$\dot{w}_r(\mathrm{j}\omega) = v_r = Y_{rp}F_p + Y_{rs}V_{cs}, \tag{20}$$

where $Y_{rp}$ and $Y_{rs}$ are the transfer functions giving the velocity at the error sensor location per unit primary force and per unit control voltage to the triangular actuator, respectively, which can be obtained by

$$Y_{rp} = \mathbf{\Phi}_r\mathbf{a}_p \quad \text{and} \quad Y_{rs} = \mathbf{\Phi}_r\mathbf{a}_s, \tag{21}$$

where $\mathbf{\Phi}_r = \mathbf{\Phi}(x_r)$, i.e.

$$\mathbf{\Phi}_r = [\phi_1(x_r) \;\; \phi_2(x_r) \;\; \ldots \;\; \phi_n(x_r)], \tag{22}$$

and $\mathbf{a}_p$ and $\mathbf{a}_s$ are given in Eq. (17).

For the direct velocity feedback control, the driving voltage, $V_{cs}$, is given by

$$V_{cs}(\mathrm{j}\omega) = -hv_r(\mathrm{j}\omega), \tag{23}$$

where $h$ is a feedback gain. Thus,

$$v_r(\mathrm{j}\omega) = \frac{Y_{rp}F_p}{1 + hY_{rs}}. \tag{24}$$

The stability analysis is carried out with reference to the Nyquist criterion which is assessed using the Bode and Nyquist plots of the sensor–actuator frequency response function, $hY_{rs}(\mathrm{j}\omega)$. Since the feedback gain is assumed to be constant, the stability can be assessed by analysing the transfer function, $Y_{rs}(\mathrm{j}\omega)$, given by

$$Y_{rs}(\mathrm{j}\omega) = \sum_{n=1}^{\infty} A_n(\mathrm{j}\omega)\phi_n(a)me_{31}^0 h_s[(m^2+3)\{\phi_n(a) - \phi_n(0)\} - a\phi_n'(0)]. \tag{25}$$

The behaviour of the sensor–actuator frequency response function thus depends on the boundary conditions ($\kappa$ and $\tau$), the shape dimensions of the triangular actuator ($a$, $b$, or $\theta_{\mathrm{PZT}}$) and the location of the sensor ($a$ in this case). The phase characteristics of the sensor–actuator frequency response function can be assessed from

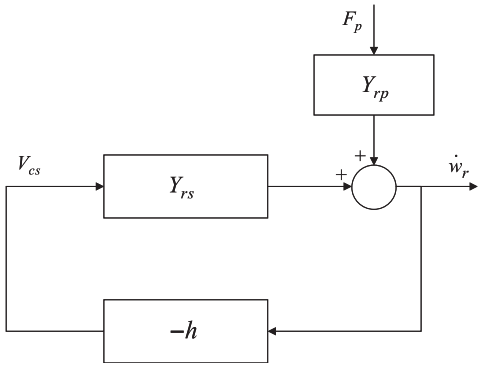


Fig. 7. Active feedback control system using a triangular shaped piezoceramic actuator.

the function

$$\Gamma_n = \phi_n(a)[(m^2+3)\{\phi_n(a)-\phi_n(0)\} - a\phi_n'(0)]. \tag{26}$$

In fact, since the phase of $A_n(\mathrm{j}\omega)$ in Eq. (25) always stays between $\pm 90^\circ$, the phase of the sensor–actuator frequency response function is shifted when the sign of $\Gamma_n$ is changed from positive to negative.

In order to facilitate the physical interpretation of the sensor–actuator frequency response function, it is useful to divide Eq. (25) into three parts for each term of actuation, that is: a point force at $x = 0$, another point force at $x = a$, a point moment at $x = 0$.

For the point force at $x = 0$,

$$Y_{f0}(a,\mathrm{j}\omega) = \sum_{n=1}^{\infty} A_n(\mathrm{j}\omega)\, me_{31}^0 h_s \phi_n(a)(m^2+3)[-\phi_n(0)], \tag{27}$$

for the point force at $x = a$,

$$Y_{fa}(a,\mathrm{j}\omega) = \sum_{n=1}^{\infty} A_n(\mathrm{j}\omega)\, me_{31}^0 h_s \phi_n(a)(m^2+3)[\phi_n(a)], \tag{28}$$

and for the point moment at $x = 0$,

$$Y_{m0}(a,\mathrm{j}\omega) = \sum_{n=1}^{\infty} A_n(\mathrm{j}\omega)\, me_{31}^0 h_s \phi_n(a)[-a\phi_n'(0)]. \tag{29}$$

So,

$$Y_{rs}(\mathrm{j}\omega) = Y_{f0}(a,\mathrm{j}\omega) + Y_{fa}(a,\mathrm{j}\omega) + Y_{m0}(a,\mathrm{j}\omega). \tag{30}$$

For this initial study, the beam is assumed to be clamped at both ends ($\kappa = \infty$ and $\tau = \infty$). The actuator's dimensions are $a = 25\,\mathrm{mm}$ and $b = 15\,\mathrm{mm}$, i.e. $\theta_{\mathrm{PZT}} = 31^\circ$. Since $\phi_n(0) = 0$ and $\phi_n'(0) = 0$ for the clamped beam, the force and moment at the end do not influence the beam and the overall effect is that of a point force at $x = a$, so that the sensor–actuator frequency response function in the case of the clamped beam can be written as

$$G(\mathrm{j}\omega) = Y_{rs}^{(cc)}(a,\omega) = \sum_{n=1}^{\infty} A_n(\mathrm{j}\omega)\, me_{31}^0 h_s (m^2+3)\,\phi_n^2(a). \tag{31}$$

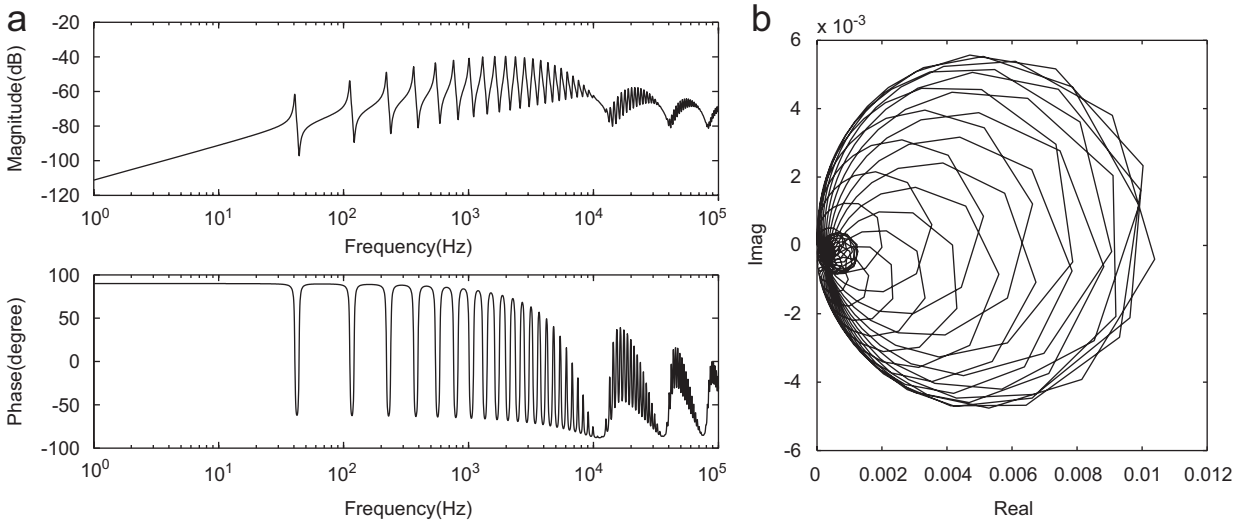


Fig. 8. Sensor–actuator frequency response function for a clamped beam from the triangularly shaped piezoceramic actuator to the velocity sensor at $x = a$. (a) Bode diagram, (b) Nyquist plot.

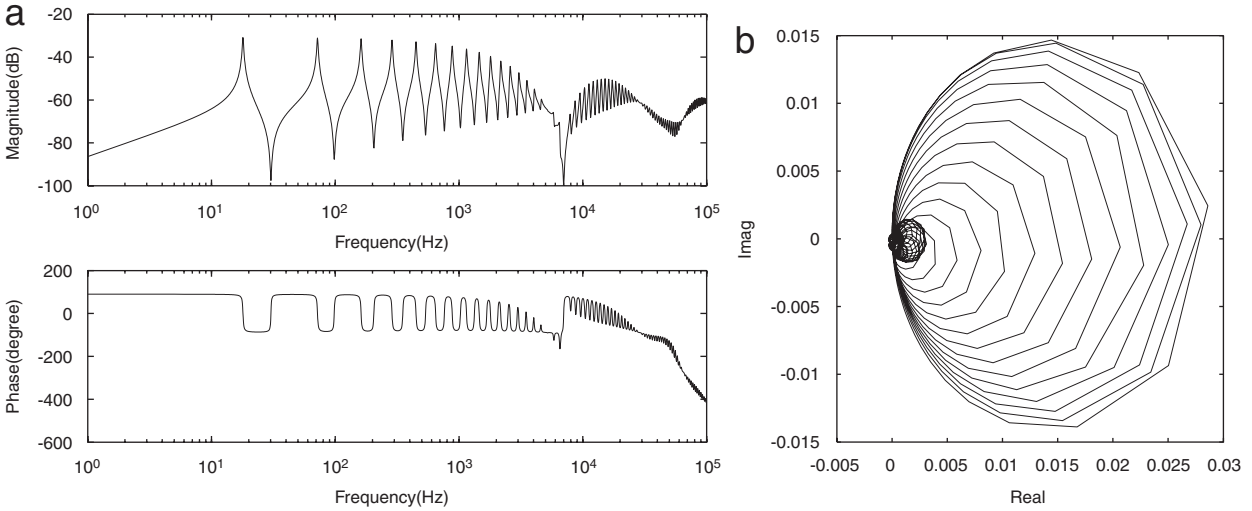


Fig. 9. Sensor–actuator frequency response function for a simply supported beam from the triangularly shaped piezoceramic actuator to the velocity sensor at $x = a$: (a) Bode diagram, (b) Nyquist plot.

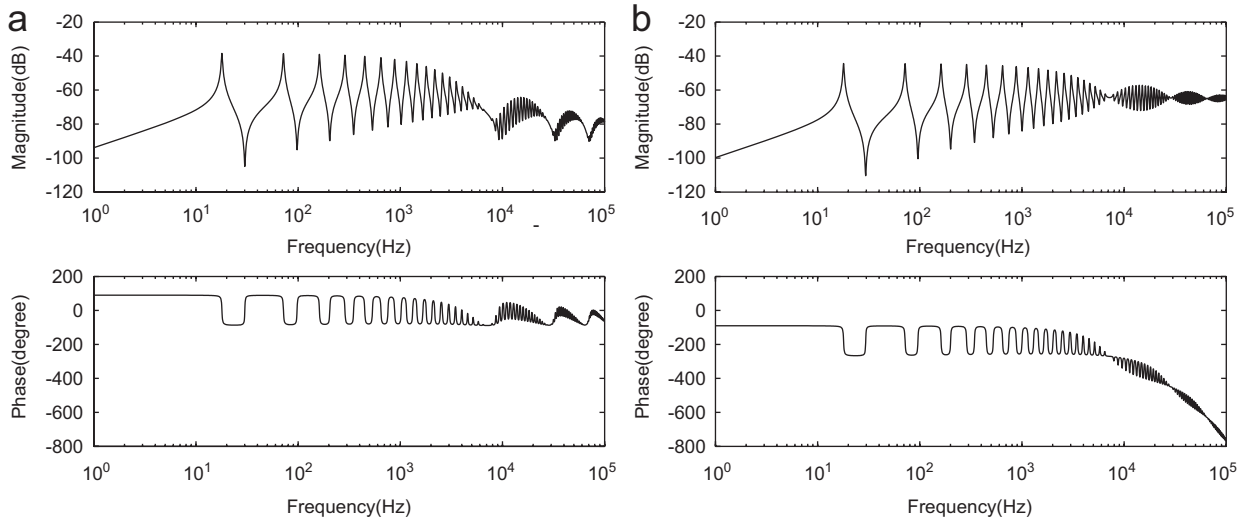


Fig. 10. Components of the sensor–actuator frequency response function for a simply supported beam from the triangularly shaped piezoceramic actuator to the velocity sensor at $x = a$: (a) due to collocated forces at $x = a$ and (b) due to moment $x = 0$.

Since $m = \tan\theta_{PZT} > 0$ for the physically possible shapes, i.e. $\theta_{PZT} < 90^\circ$, it can be expected that the phase of the plant response always stays between $\pm 90^\circ$, and so the control system is to be *unconditionally stable*.[1] Indeed, Fig. 8 shows that the phase of $G(j\omega)$ is confined between $\pm 90^\circ$ so that the locus stays in the right-hand side, which indicates that the control system is unconditionally stable. The dips in the sensor–actuator frequency response function which are due to nodes of modes occurring close to the sensor location can be found at about 10, 40 and 80 kHz. Those frequencies correspond to the $n$th natural frequencies such that the first, second or third nodal point of the $n$th mode coincides to the height of actuator, $a$. Those frequencies decrease as the stiffness of the boundary, $\kappa$ and/or $\tau$ are decreased since the corresponding nodal points occurs

[1]However, it should be noted that the distributed moments along the lateral edges of the actuator can couple into the transverse plate modes so that unconditional stability is not any more guaranteed.

at lower modes. The frequency of these drops can be obtained explicitly for a simply supported beam since the coordinate of the first nodal point of the $n$th mode can be expressed as $L/n$ for $n \geqslant 2$.

When the beam is simply supported ($\kappa = \infty$ and $\tau = 0$), $\phi_n(0) = 0$ but $\phi'_n(0) \neq 0$. The moment at $x = 0$ couples into the modes while the force at $x = 0$ does not. Since the moment couples more efficiently into higher modes, an extra phase shift occurs at a higher frequency. Fig. 9 shows the sensor–actuator frequency response function in the case of a simply supported beam. It can be seen that the control system is only conditionally stable but the gain margin is about 65 dB. The conditional stability is due to the existence of the non-collocated, non-dual moment actuation at $x = 0$. The total response at the sensor location is given by the sum of the response due to the concentrated forces at $x = a$ shown in Fig. 10 (a) and the response due to the concentrated moment at $x = 0$ shown in Fig. 10(b). At frequencies below 7 kHz, the two responses are out-of-phase but the magnitude due to the forces is much bigger than the other. The phase of the total response shown in Fig. 9 stays between $\pm 90^\circ$ in this frequency range. Around 7 kHz, however, the response due to the force decreases because resonating modes at these frequencies have nodal lines close to the tip of the triangular actuator where both actuation and velocity sensing occurs. This leads to a small response and also inefficient actuation. Since the moment excitation component is located at the end of the beam and couples efficiently into higher order modes, the response due to the moment excitation component remains relatively large at higher frequencies. However, the total response at higher frequencies where the phase exceeds $-90^\circ$ is still small compared to the low frequency where the phase is between $\pm 90^\circ$ so that a large gain margin is available.

One possible way to remove the phase shift is to increase the rotational spring constant. In Eq. (25), $\phi'_n(0)$ decreases as $\tau$ increases so that the phase of the sensor–actuator frequency response function is shifted with a smaller magnitude at a higher frequency. It is noted, however, that the sensor–actuator frequency response function is decreased at low frequencies as the rotational spring constant increases because $\phi_n(0) \to \phi_n(a)$ and $\phi'_n(0) \to 0$ at low frequencies.

A freely supported beam such that $\kappa = 0$ and $\tau = 0$ is now considered. For this case, $\phi_n(0) \neq 0$ and $\phi'_n(0) \neq 0$, and so the sensor–actuator frequency response function is given by Eq. (25). The plots in Fig. 11 for this case display a marked instability effect. When $\kappa \to 0$, $\phi_n(a) \approx \phi_n(0)$ (assuming $\phi_n(a) > 0$) at frequencies less than $n$th natural frequency ($f < f_n$) such that $n \approx L/a$. Therefore $Y_{rs}(\omega) \to 0$, where $f_n$ is about 2 kHz in this case. Precisely, at frequencies such that $\phi_n(a) < \phi_n(0)$, the phase of the sensor–actuator frequency response function is thus outside the range of $\pm 90^\circ$. This is because at low frequencies the contribution of the forces at $x = 0$ to the sensor response is slightly higher and with opposite phase than that of the force at $x = a$. The total sensor–actuator frequency response function is hence characterised by a phase outside the $\pm 90^\circ$ range at low frequencies. In order to obtain a higher gain margin, the contribution of the forces at $x = 0$ to the

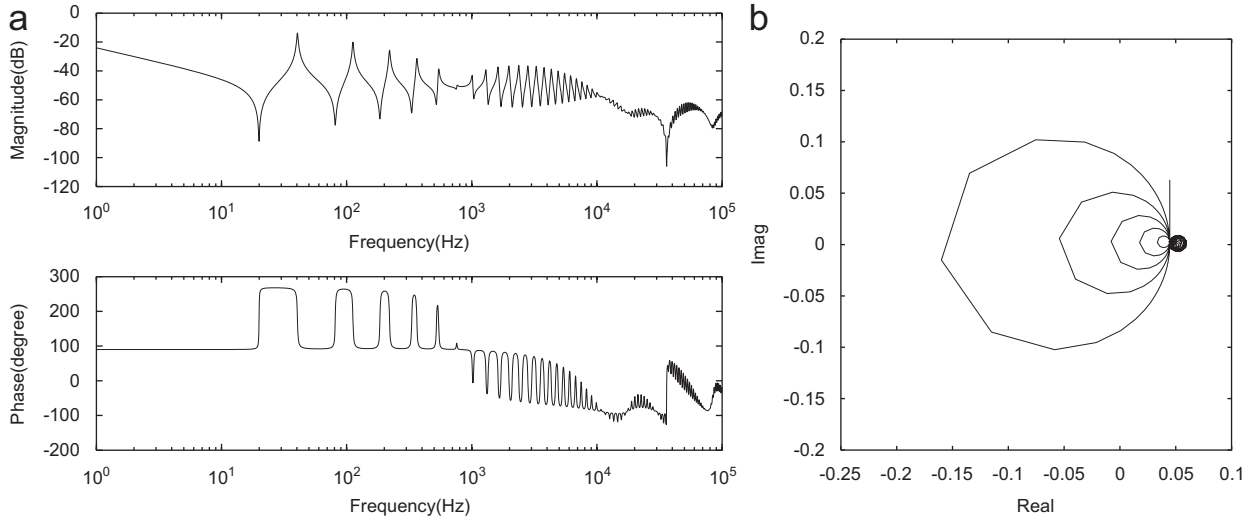


Fig. 11. Sensor–actuator frequency response function for a freely supported beams ($\tau = 0$ and $\kappa = 0$) from the triangularly shaped piezoceramic actuator to the velocity sensor at $x = a$: (a) Bode diagram, (b) Nyquist plot.

sensor–actuator frequency response function at the sensor location should be reduced by increasing the linear spring constant.

The rotational spring at the boundary affects the frequency response only at the dips caused by the height of the actuator. However, the influence is not critical because a high gain margin can still be obtained. In contrast the linear spring significantly affects the stability at low frequencies up to about the $n$th natural frequency where the first nodal point of the $n$th mode reaches the tip of the actuator. The stiffness necessary to guarantee closed loop stability can be found for a given beam and actuator. Although it is possible to obtain a higher gain margin with a higher linear spring constant and/or a higher rotational spring constant, the control

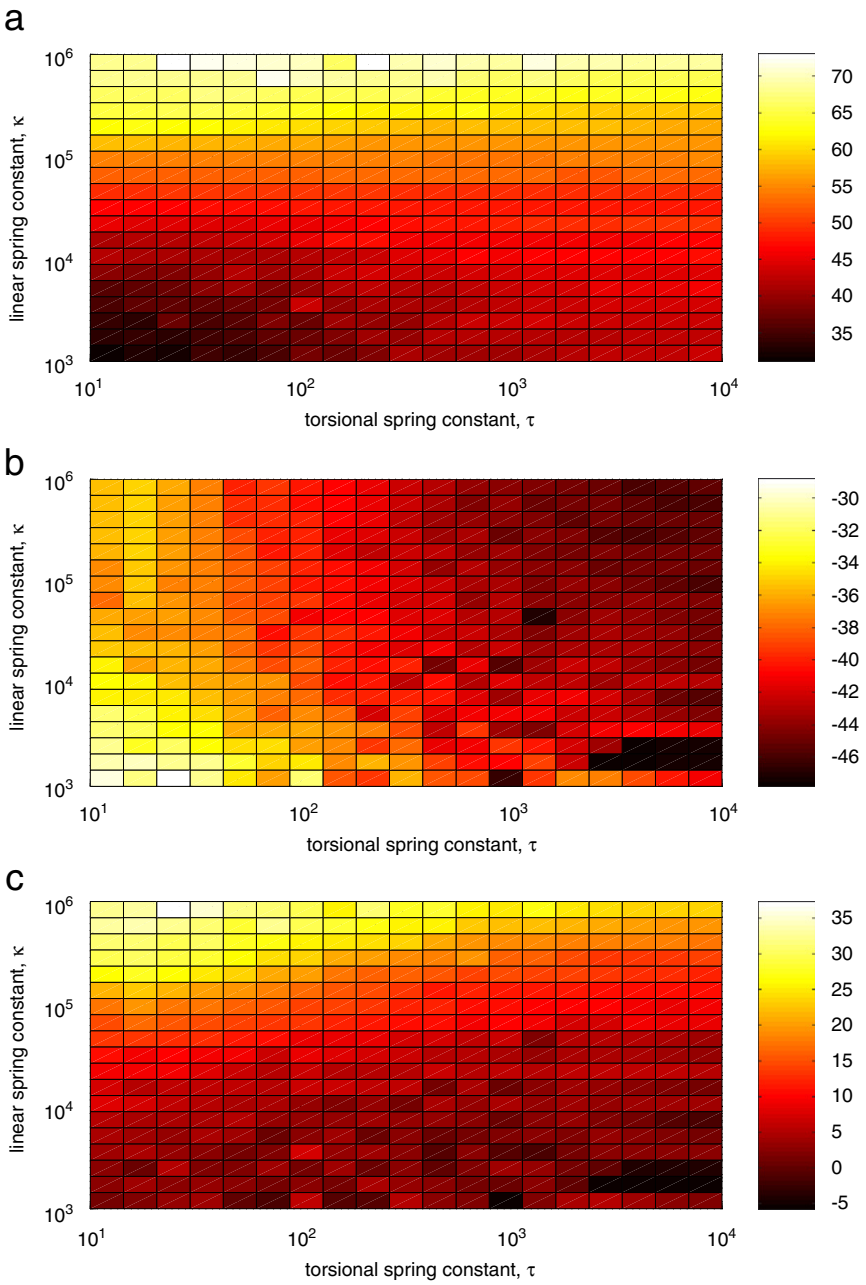


Fig. 12. (a) Maximum gain margin (dB), (b) maximum sensor–actuator frequency response function (dB), and (c) performance index (dB) with respect to the spring constants.

performance depends on the amplitude of the sensor–actuator frequency response function. Since the rotational spring tends to reduce the amplitude of the sensor–actuator frequency response function, there exists an optimal value for the best trade-off between stability and control performance. To describe this effect, a performance index (PI) is defined as

$$\mathrm{PI} = 20\log_{10}(\mathrm{GM}\cdot\mathrm{PR}) \quad (\mathrm{dB}), \tag{32}$$

where GM is the gain margin and PR is the maximum positive real part of $G(j\omega)$, i.e. $\max(\mathrm{Re}\{G(j\omega)\})$. The maximum attenuation is then given by $20\log_{10}(1+\mathrm{GM}\cdot\mathrm{PR})$ in dB.

Fig. 12 shows the variation of these three values in terms of linear and rotational spring constants. It can be seen from Fig. 12(a) that, at low linear spring constants up to $\kappa = 10^4$, the rotational spring helps to increase the gain margin while at higher linear spring constants the rotational spring does not affect the gain margin. It can be also seen from Fig. 12(b) that, at low rotational spring constants up to $\tau = 10^2$, the linear spring decreases the maximum sensor–actuator frequency response function, while at higher rotational spring constants the linear spring does not affect the maximum amplitude of the sensor–actuator frequency response function. Therefore, as shown Fig. 12(c), the performance index is increased as the linear spring constant increases while it is decreased at $\tau = 50$ when $\kappa = 10^6$ as the rotational spring constant increases. Note, however, that the torsional stiffness when $\tau = 50$ is relatively low such that it does couple into few modes as shown in Fig. 2(b). The active control system using a triangularly shaped piezoceramic actuator can thus yield a reasonable performance for a beam with practical boundary condition with a high linear spring constant, i.e. $\kappa \gtrsim 10^4$, which corresponds to an almost simply supported boundary condition for the first six flexural modes, as shown in Fig. 2(a).

## 5. Control performance

This section considers the performance of a direct velocity feedback control system using a triangularly shaped piezoceramic actuator bonded at the left hand side of a resiliently mounted beam with a velocity sensor at the vertex of the actuator (Fig. 1). The effect of the boundary condition is examined first using the actuator shape of $a = 25\,\mathrm{mm}$ and $b = 15\,\mathrm{mm}$.

Fig. 13 shows the performance in terms of the total kinetic energy of a clamped beam, so that the feedback loop is unconditionally stable, excited by a concentrated force at $x = 0.8L$ when subject to the feedback control system with gains of $10^3, 10^4$ and $10^5$. It can be seen that, as the feedback gain is increased, the total kinetic energy decreases at resonance frequencies. Increasing the feedback gain further, however, begins to increase the response at other resonant frequencies because the control action, which is a force in this case, is

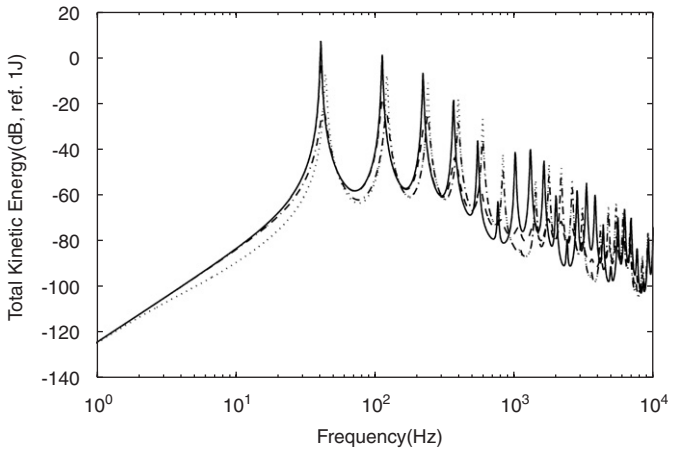


Fig. 13. Total kinetic energy of a clamped beam excited by a concentrated force at $0.2L$ (solid) and subjected to the direct velocity feedback control using a triangularly shaped piezoceramic actuator ($a = 25\,\mathrm{mm}$, $b = 15\,\mathrm{mm}$) with the feedback gains of $10^3$ (dashed), $10^4$ (dot–dashed) and $10^5$ (dotted).

high enough to pin the beam at the error sensor position so that a new boundary condition is introduced [18]. Therefore, the control system has a best performance at an optimal gain where the control system produces the maximum damping effect without pinning effect. The performance is relatively poor at low frequencies because of small sensor–actuator frequency response function when the beam is clamped. Fig. 14 shows the control performance for a simply supported beam under the same control system. Better performance than with the clamped beam can be achieved with a smaller feedback gain although the feedback loop is now only conditionally stable. The feedback gains used in the simulation are 100, 1000 and 2000. It should be noted that the control system for a simply supported beam is only conditionally stable. The maximum gain in this case is about 2000, which is obtained from Fig. 9. Control spillover occurs between 5 and 7 kHz as predicted in the sensor–actuator frequency response function shown in Fig. 9. Fig. 15 shows the control performance of the direct velocity feedback control of a resiliently mounted ($\kappa = 10^5$ and $\tau = 0$) beam with the feedback gains of 100, 300 and 600 (maximum gain). The control performance is almost the same as that for simply supported beam except for the maximum gain and the control spillover occurred between 3 and 4 kHz.

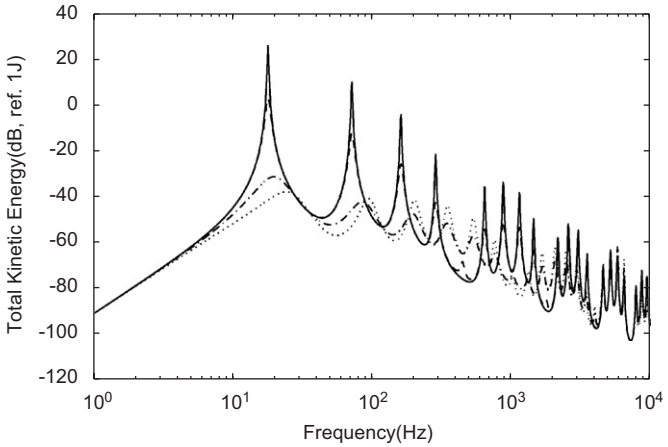


Fig. 14. Total kinetic energy of a simply supported beam excited by a concentrated force at $0.2L$ (solid) and subjected to the direct velocity feedback control using a triangularly shaped piezoceramic actuator ($a = 25$ mm, $b = 15$ mm) with the feedback gains of $10^2$ (dashed), $10^3$ (dot–dashed) and $2 \times 10^3$ (dotted).

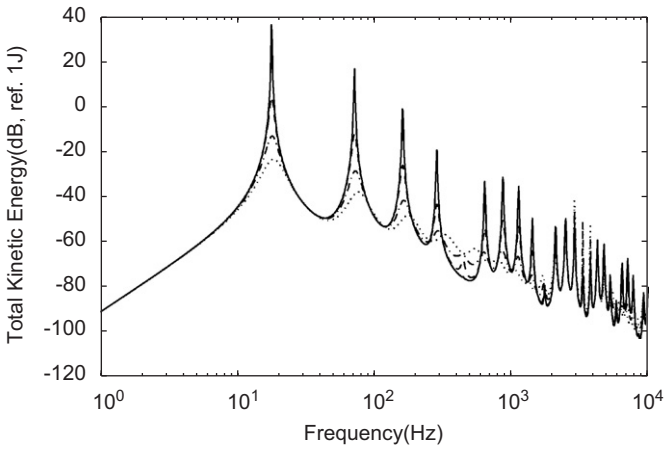


Fig. 15. Total kinetic energy of a resiliently mounted ($\kappa = 10^5$ and $\tau = 0$) beam excited by a concentrated force at $0.2L$ (solid) and subjected to the direct velocity feedback control using a triangularly shaped piezoceramic actuator ($a = 25$ mm, $b = 15$ mm) with the feedback gains of 100 (dashed), 300 (dot–dashed) and 600 (dotted).

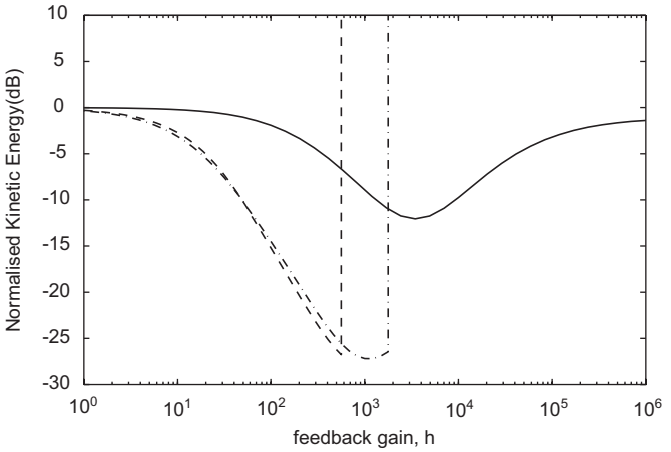


Fig. 16. Variation of the normalised average kinetic energy, integrated up to 2 kHz, with the feedback gain from 1 to $10^6$ for clamped beam (solid line), simply supported beam (dot–dashed line) and resiliently mounted beam ($\kappa = 10^5$ and $\tau = 0$) (dashed line), of beams using a triangularly shaped piezoceramic actuator ($a = 25$ mm, $b = 15$ mm).

The overall performance of the control systems can be evaluated in terms of the normalised kinetic energy given by

$$\overline{\mathrm{KE}}(h) = 10\log_{10}\frac{\int_{f_1}^{f_2}\mathrm{KE}(f,h)\,\mathrm{d}f}{\int_{f_1}^{f_2}\mathrm{KE}_p(f)\,\mathrm{d}f}, \quad \mathrm{dB} \tag{33}$$

where $\overline{\mathrm{KE}}$ represents the normalised average kinetic energy. KE and $\mathrm{KE}_p$ are the kinetic energies before and after control, respectively. $f_1$ and $f_2$ are the lower and upper frequencies of the frequency range of interest.

The normalised performance, integrated up to 2 kHz, is compared in Fig. 16 for the three boundary conditions: clamped, simply supported and resiliently mounted. The normalisation is performed in the frequency range between 0 and 2 kHz. It can be seen that a maximum reduction in the kinetic energy of the clamped beam is restricted to 10 dB by the pinning effect of the feedback loop with high gains. The control system for the simply supported beam gives much higher reduction of 27 dB in the kinetic energy and is limited by the maximum gain that can be used for this conditionally stable case. For the practical boundary condition ($\kappa = 10^5$ and $\tau = 0$), a reduction of 26 dB in the kinetic energy can be achieved. It is therefore clear that the practical boundary condition should have a high linear spring stiffness in order to obtain a good control performance of active control systems using a triangular actuator.

## 6. Parametric study

The stability and the control performance are affected by the shape of the actuator. The shape of the actuator can be defined by the height of the triangular actuator, $a$, and its half-top angle, $\theta_{\mathrm{PZT}}$. Effects of these parameters of the triangular actuator on the control system are investigated for the resiliently mounted beam ($\kappa = 10^5$ and $\tau = 0$).

### 6.1. Effect of the top angle of the actuator

The effects of the top angle of a triangular actuator is examined first keeping the height to be constant. The sensor–actuator frequency response function varies with the location of the velocity sensor, which corresponds to the height of the actuator in this case. The actuator shapes considered are shown in Fig. 17 with the top angles of $\theta_{\mathrm{PZT}} = 15^\circ, 30^\circ, 45^\circ, 60^\circ$ and $75^\circ$. The width of the beam is assumed to be as large as the width of the base of the triangular actuator while keeping the bending rigidity to be constant. The ratio of the actuation resultants hence depends only on the angle for the given beam and actuator materials as shown in Fig. 6.

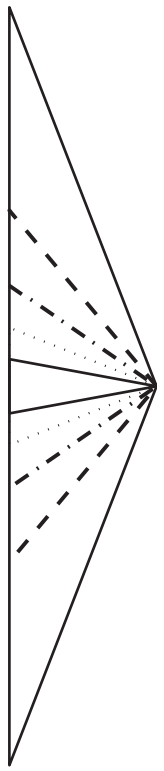

Fig. 17. Actuator shapes varied with the top angles of $\theta_{PZT} = 15°, 30°, 45°, 60°, 75°$. The boundary condition of the beam is that $\kappa = 10^5$ and $\tau = 0$.

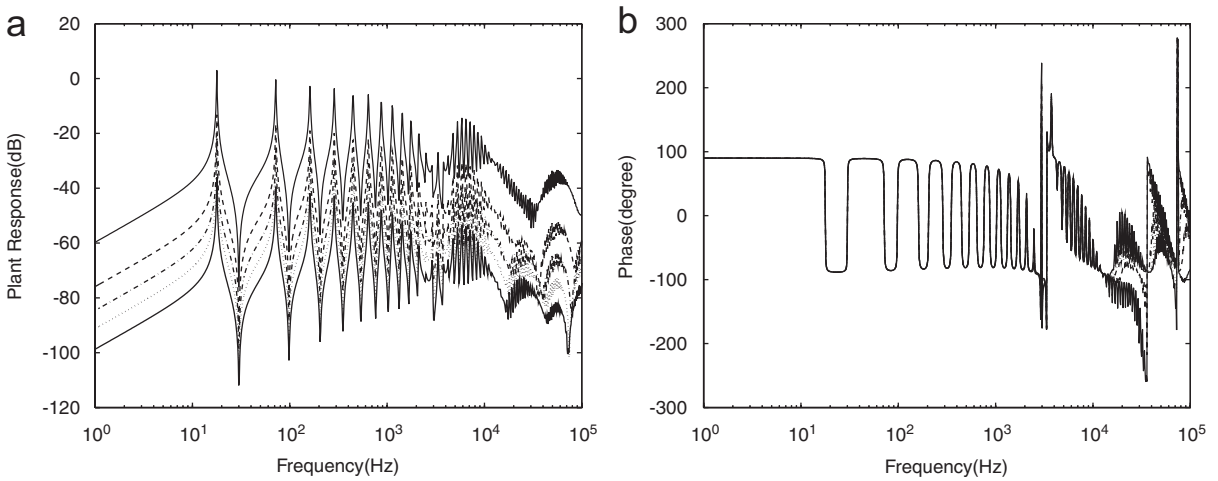


Fig. 18. Variation of the sensor–actuator frequency response function with the top angles of the triangularly shaped piezoceramic actuator. The boundary condition of the beam is that $\kappa = 10^5$ and $\tau = 0$: (a) magnitude (dB), (b) phase (degree).

The sensor–actuator frequency response functions are calculated for the five shapes and shown in Fig. 18. It is found that the magnitude of the sensor–actuator frequency response function increase monotonically as increasing $\theta_{PZT}$ and the phase characteristics is the same up to the frequency where the moment along the base of the actuator begins to affect the total response, which is about 3 kHz in this case. The gain margin thus decreases while the maximum amplitude of the sensor–actuator frequency response function increases as $\theta_{PZT}$

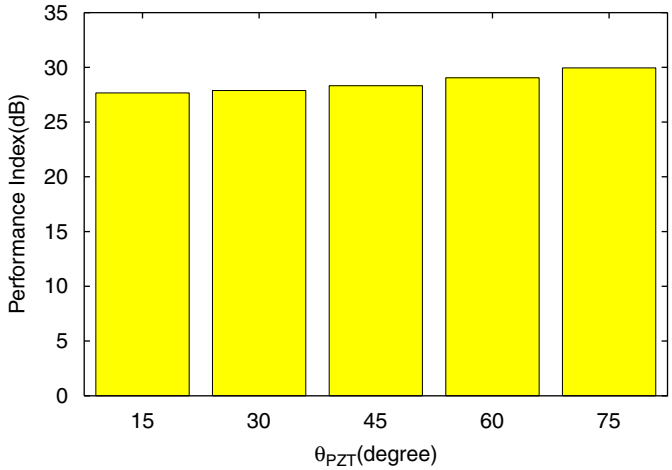


Fig. 19. Variation of the performance index with the top angle of the triangularly shaped piezoceramic actuator. The boundary condition of the beam is that $\kappa = 10^5$ and $\tau = 0$.

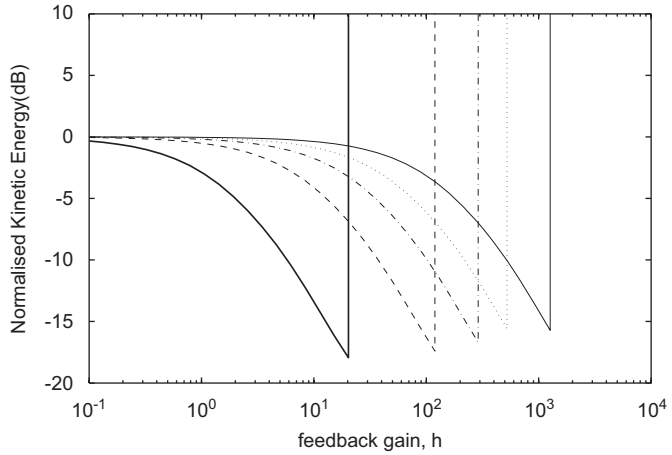


Fig. 20. Effect of the actuator's top angle on the normalised kinetic energy with the feedback gain from 0.1 to $10^4$ for the resiliently mounted ($\kappa = 10^5$ and $\tau = 0$) beam using a triangularly shaped piezoceramic actuator with $b = 15$ mm and $\theta_{PZT} = 15^\circ$ (thick solid), $\theta_{PZT} = 30^\circ$ (dotted), $\theta_{PZT} = 45^\circ$ (dot–dashed), $\theta_{PZT} = 60^\circ$ (dashed), $\theta_{PZT} = 75^\circ$ (solid).

increases, so that the performance index, as defined in Eq. (32), is almost the same, which is between 27 and 30 dB as shown in Fig. 19.

Fig. 20 shows the effect of the actuator's top angle on the normalised kinetic energy, integrated up to 2 kHz as a function of feedback gain. With this actuator shape variation, the same reduction of 15 dB in the kinetic energy can be achieved at increasing feedback gains as the width is reduced. It can be seen that the feedback gain for approximately the same maximum performance is decreased as the top angle is decreased, so that the actuator with wider angle is preferable because the control effort is lower.

### 6.2. *Effect of the size of the actuator*

In practical systems, the width of the actuator is limited to that of the beam and the height of actuator should be in the range of values such that the force generated at the vertex can couple into the beam modes up

to the frequency of interest and the sensor at the vertex can respond. The effect of the actuator's size is hence examined with three different heights of the actuator with the same top angle having $\theta_{PZT} = 37^\circ$ and the height of 5, 10 and 20 mm, as shown in Fig. 21, which correspond to 1%, 2% and 4% of the beamlength ($L = 0.5$ m).

The sensor–actuator frequency response functions are calculated for the 0.5 m long beam and shown in Fig. 22. The response increases as the size of actuator increases at low frequencies, but the bigger actuator leads to the instability at lower frequency. The actuator height is hence limited by the frequency range where the reduction should be guaranteed. The performance index is obtained again for the actuators as shown in Fig. 23. It can be seen that the performance index is very small when the actuator size is small. This is because the force generated by the actuator at the vertex could not couple into the structure effectively while the moment generated along the base of the actuator can couple into it.

Fig. 24 shows the normalised kinetic energy, integrated up to 2 kHz, with the feedback gain from 0.1 to $10^4$ using the triangularly shaped piezoceramic actuators. It can be found that the maximum gains that guarantee

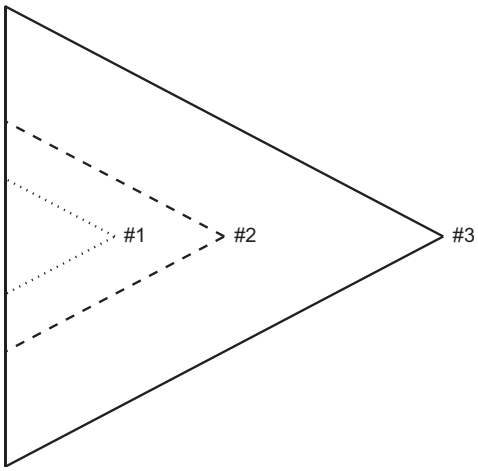


Fig. 21. Three different sizes of the actuators with the same shapes having $\theta_{PZT} = 37^\circ$ and the height of 5, 10 and 20 mm. The boundary condition of the beam is that $\kappa = 10^5$ and $\tau = 0$.

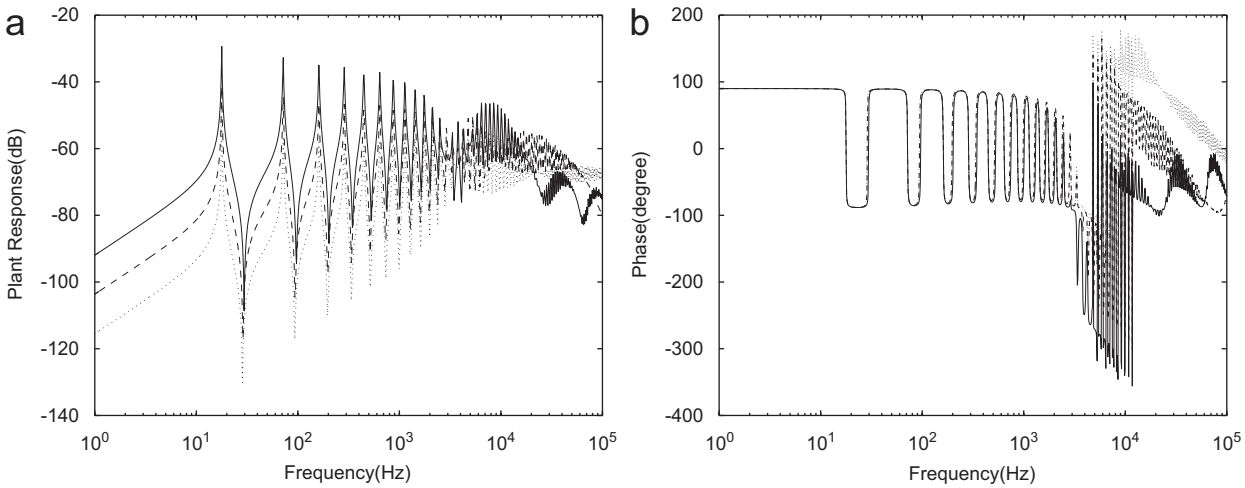


Fig. 22. Variation of the sensor–actuator frequency response function with the sizes of the triangularly shaped piezoceramic actuator. The boundary condition of the beam is that $\kappa = 10^5$ and $\tau = 0$: (a) magnitude (dB), (b) phase (degree).

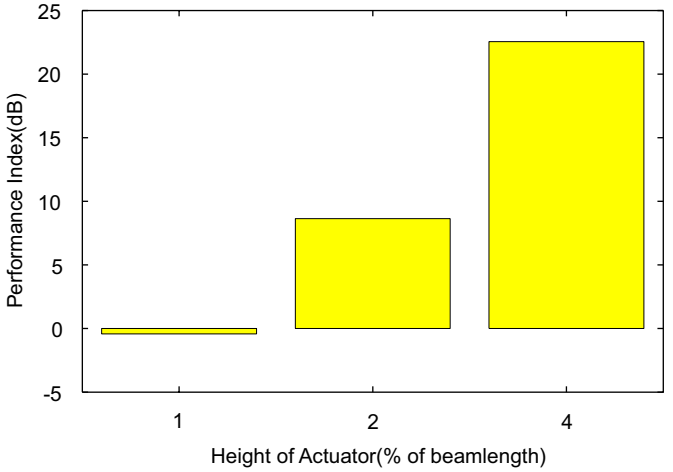


Fig. 23. Variation of the performance index with the size of the triangularly shaped piezoceramic actuator on a 0.5 m long beam. The boundary condition of the beam is that $\kappa = 10^5$ and $\tau = 0$.

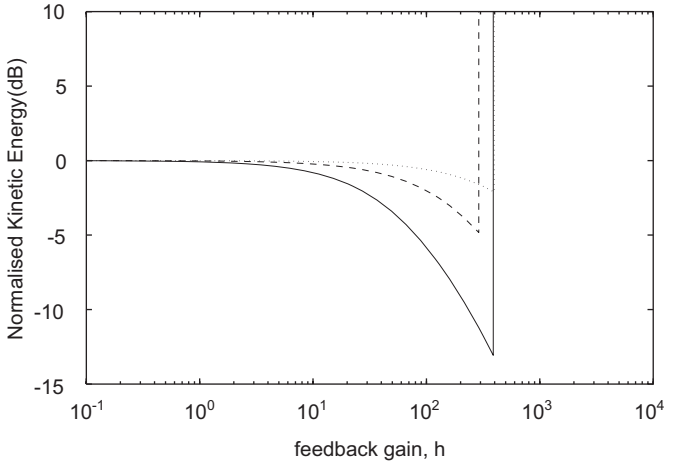


Fig. 24. Effect of the actuator shape on the normalised kinetic energy with the feedback gain from 0.1 to $10^4$ for the resiliently mounted ($\kappa = 10^5$ and $\tau = 0$) beam using a triangularly shaped piezoceramic actuator with $\theta_{PZT} = 37^\circ$ and $a = 5$ mm (solid), 10 mm (dashed) and 20 mm (dotted).

stability are almost the same, which is between 300 and 400, while the reduction performance is much different from each other. The reduction performance is increased as the size of the actuator is increased.

### 6.3. *Effect of the shape of the actuator*

For further investigation of height effect, four different actuators as shown in Fig. 25 are now considered. They have the same base, $b = 15$ mm, but have different heights of 20, 50, 100 and 200 mm, corresponding to $\theta_{PZT} = 37^\circ, 16.5^\circ, 8.5^\circ$ and $4.3^\circ$. Fig. 26 shows that the magnitude of the sensor–actuator frequency response functions at low frequencies up to 500 Hz increases as the height of the actuator increases, while it decreases up to 2 kHz. This is because of the variation of the dominant actuation effect between the force and moment generated by the actuator for a given height. Another important feature is the cut-off frequency where the phase leg exceeds $-90^\circ$. This frequency decreases as the height of the actuator increases. For the cases considered here, those frequencies are at 4, 3, 2 kHz and 800 Hz. The variation of the performance index shown in Fig. 27 with the different height of actuator reflects all these behaviours. When the actuator is too

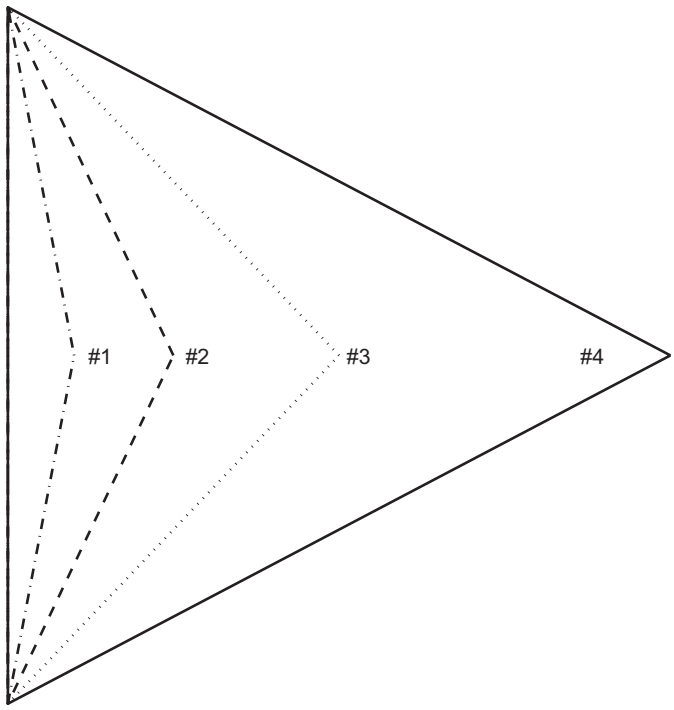


Fig. 25. Four different shapes of the actuators having $a = 20\,\text{mm}, 50, 100$ and $200\,\text{mm}$ with the same base of $30\,\text{mm}$.

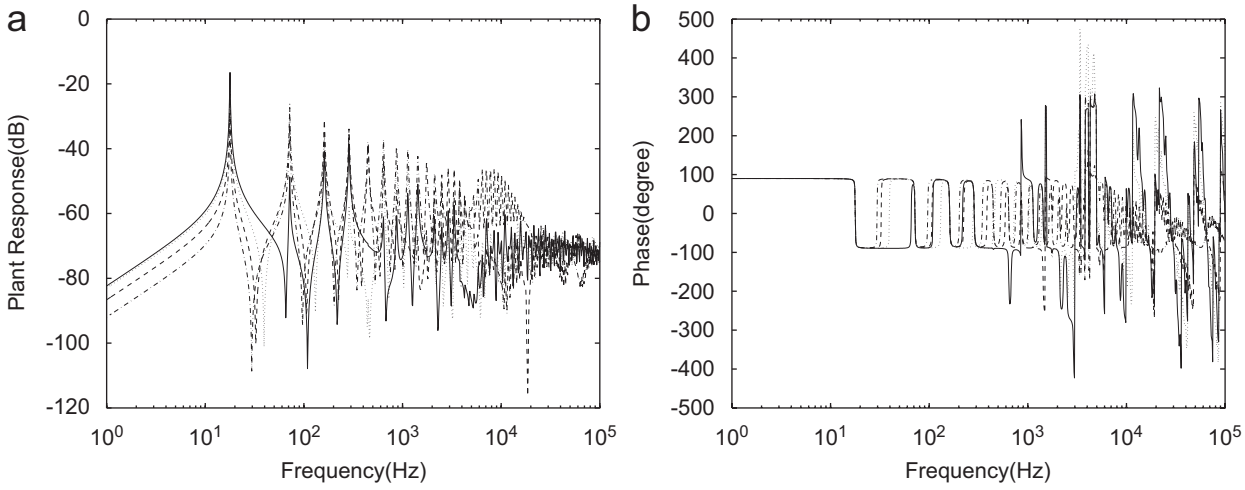


Fig. 26. Variation of the sensor–actuator frequency response function with the size of the triangularly shaped piezoceramic actuator. The boundary condition of the beam is that $\kappa = 10^5$ and $\tau = 0$: (a) magnitude (dB), (b) phase (degree).

small, the force does not couple into the modes efficiently so that the performance index is rather low. When the actuator is too large, the phase shift occurs at rather low frequency so that the performance index becomes relatively small.

The variation of the performance with the shapes are not consistent as shown in Fig. 28. This is due to the contrasting effects generated by the simultaneous variation of angle and height as the top angle increased. Therefore, we can consider an optimal shape for a given base of actuator and the frequency range. Considering the four shapes of the actuator, the best performance can be achieved using the intermediate shape #3.

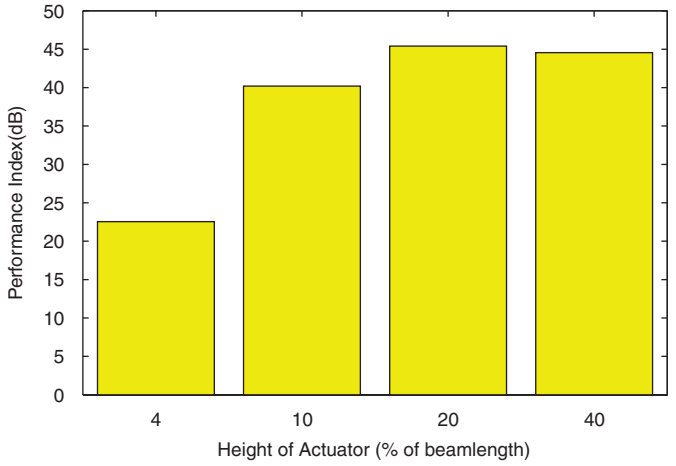


Fig. 27. Variation of the performance index with the size of the triangularly shaped piezoceramic actuator. The boundary condition of the beam is that $\kappa = 10^5$ and $\tau = 0$.

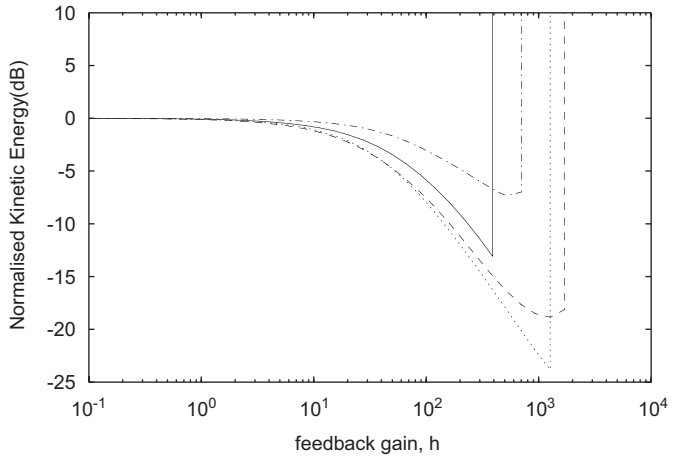


Fig. 28. Effect of the actuator shape on the normalised kinetic energy with the feedback gain from 0.1 to $10^4$ for the resiliently mounted ($\kappa = 10^5$ and $\tau = 0$) beam using a triangularly shaped piezoceramic actuator with $b = 15$ mm and $a = 20$ mm (solid), 50 mm (dashed), 100 mm (dotted) and 200 mm (dot–dashed).

## 7. Conclusion

This paper is concerned with triangularly shaped actuators for the implementation of direct velocity feedback control systems on resiliently mounted beams. Effects of boundary conditions and the shape of the actuator on the control system are mainly investigated. For practical boundary conditions given by a combination of the rotational and linear springs, it is found that the linear spring is the most important component necessary to achieve collocated sensing and actuation in a desired frequency range, while the rotational spring is not as important.

The dynamics of resiliently mounted beam supported by both torsional and linear springs at both ends is presented and the direct velocity feedback control of the beam using the triangularly shaped piezoceramic actuator positioned at either ends of the beam with velocity sensors at the top vertices is then investigated. It is found that the control system is influenced by the boundary condition of the beam. The shape of the actuator also affects the stability and the performance of the control system. When the beam is clamped, the triangularly shaped actuator is perfectly collocated and dual with the velocity sensor at the tip so that the

control system is unconditionally stable. In terms of performance, however, the control system for a simply supported beam is better than for the clamped beam although the system is only conditionally stable in this case. For practical boundary conditions achieved by the combination of the torsional and linear springs, the linear spring is the most important component to effectively achieve collocation in a desired frequency range.

The effect of the shape of actuator is also investigated. The magnitude of the sensor–actuator frequency response function is increased as the top angle is increased while the phase is not changed much. A smaller feedback gain should be used with the wider actuator, thus saving control effort. The effect of the actuator size is to increase the sensor–actuator frequency response functions as the size of the actuator is increased, although the gain margin is also slightly reduced. Finally, as the base is fixed and the height is changed, so that the top angle is also changed, the performance increases with height until it becomes about 20% of the length of the beam.

## References

[1] F.J. Fahy, *Sound and Structural Vibration*, Academic Press, London, 1994.
[2] P. Gardonio, S.J. Elliott, Smart panels with velocity feedback control systems using triangularly shaped strain actuators, *Journal of Acoustical Society of America* 117(4) (2005) 2046–2064.
[3] C. Hong, S. J. Elliott, Active control of resiliently-mounted beams with a moment pair actuator, *Smart Materials and Structures* 14(2005) 727–738.
[4] P. Gardonio, E. Bianchi, S.J. Elliott, Smart panel with multiple decentralized units for the control of sound transmission. Part I. Theoretical predictions, *Journal of Sound and Vibration* 274 (2004) 163–192.
[5] P. Gardonio, E. Bianchi, S.J. Elliott, Smart panel with multiple decentralized units for the control of sound transmission. Part II. Design of decentralized control units, *Journal of Sound and Vibration* 274 (2004) 193–213.
[6] E. Bianchi, P. Gardonio, S.J. Elliott, Smart panel with multiple decentralized units for the control of sound transmission. Part III. Control system implementation, *Journal of Sound and Vibration* 274 (2004) 215–232.
[7] S.E. Burke, J. James, E. Hubbard, Active vibration control of a simply supported beam using a spatially distributed actuator, *IEEE Control Systems Mogozrne* (1987) 25–30.
[8] L. Meirovitch (Ed.), *Observability of a Bernoulli–Euler Beam Using $PVF_2$ as a Distributed Sensor*, VPI&SU, Blacksburg, VA, 1987.
[9] Y.-S. Lee, S.J. Elliott, P. Gardonio, Matched piezoelectric double sensor/actuator pairs for beam control, *Smart Materials and Structures* 12 (2003) 541–548.
[10] C.K. Lee, Theory of laminated piezoelectric plates for the design of distributed sensors/actuators. Part I. Governing equations and reciprocal relationships, *Journal of Acoustical Society of America* 87 (3) (1990) 1144–1158.
[11] J.M. Sullivan, J.J.E. Hubbard, S.E. Burke, Distributed sensor/actuator design for plates: spatial shape and shading as design parameters, *Journal of Sound and Vibration* 203 (3) (1997) 473–493.
[12] S.S. Rao, *Mechanical Vibrations*, Addison-Wesley Publishing Company Inc., Reading, MA, 1970.
[13] E.B. Magrab, *Vibrations of Elastic Structural Members*, Sijthoff and Noordhoff International Publishers B.V., 1979.
[14] S.J. Elliott, P. Gardonio, T.C. Sors, M.J. Brennan, Active vibroacoustic control with multiple local feedback loops, *The Journal of the Acoustical Society of America* 111 (2) (2002) 908–915.
[15] J.M. Sullivan, J. James, E. Hubbard, S.E. Burke, Modeling approach for two-dimensional distributed transducers of arbitrary spatial distribution, *Journal of Acoustical Society of America* 99 (5) (1996) 2965–2974.
[16] P. Gardonio, M.J. Brennan, On the origins and development of mobility and impedance methods in structural dynamics, *Journal of Sound and Vibration* 249 (3) (2002) 557–573.
[17] W.T. Thompson, *Theory of Vibration with Applications*, Prentice-Hall, New Jersey, 1981.
[18] P. Gardonio, S.J. Elliott, Modal response of a beam with a sensor–actuator pair for implementation of velocity feedback control, *Journal of Sound and Vibration* 284 (2005) 1–22.